Scilight

Environmental Science and Geoscience
https://www.sciltp.com/journals/esg

Article

The Crucial Role of Support in the Pd/MO Catalyst for SO_2 Resistance during Toluene Combustion

Gehui Wang [1], Junrong Lai [1], Zhengxuan Zhu [1], Haiqin Wan [1,2,*] and Lin Dong [1,2]

[1] State Key Laboratory of Water Pollution Control and Green Resource Recycling, School of Environment, Nanjing University, Nanjing 210023, China
[2] Jiangsu Key Laboratory of Vehicle Emissions Control, Nanjing 210023, China
* Correspondence: wanhq@nju.edu.cn; Tel.: +86-25-89680369

How To Cite: Wang, G.; Lai, J.; Zhu, Z.; et al. The Crucial Role of Support in the Pd/MO Catalyst for SO_2 Resistance during Toluene Combustion. *Environmental Science and Geoscience* **2026**, *1*(1), 2.

Received: 1 February 2026
Revised: 8 April 2026
Accepted: 10 April 2026
Published: 22 April 2026

Abstract: Developing sulfur tolerance catalyst for combustion of volatile organic compounds (VOCs) is of great significance in the removal of industrial waste gas. In this work, the roles of support over Pd-based catalyst for the sulfur tolerance during toluene oxidation were investigated by loading 0.5 wt% Pd onto CeO_2, Al_2O_3, TiO_2, and SiO_2 with or without SO_2 pretreatment. Results showed that the Pd/CeO_2 displays an attractive toluene conversion of 90% at 220 °C, outperforming other supported Pd catalysts, especially the Pd/TiO_2 catalyst (with a T_{90} of 253 °C). However, after SO_2 pretreatment, the toluene oxidation performance of Pd/TiO_2 ranked first, and its T_{90} was 38 °C lower than that of Pd/CeO_2. Characterization results indicated that the Pd^0 active species on the CeO_2 surface is highly prone to reacts with SO_2 to form stable $Ce_2(SO_4)_3$ deposition. Additionally, the decrease in activated oxygen capacity inhibits its redox performance. These factors collectively result in poor sulfur resistance of Pd/CeO_2. While the outstanding sulfur resistance of Pd/TiO_2 was closely linked to the ready decomposition of sulfates on its surface. This work elucidates the critical role of the support in dictating catalytic performance and anti-poisoning capability, thereby offering new perspectives for the design of high-performance Pd-based catalysts for VOC remediation.

Keywords: toluene oxidation; Pd-based catalysts; SO_2 poisoning; support effects; sulfur tolerance

1. Introduction

Volatile organic compounds (VOCs) are defined as organic carbon-based chemicals that typically feature low boiling points (below 260 °C), enabling them to readily volatilize under standard conditions [1]. VOCs in air pollutants can react with nitrogen oxides (NO_x), sulfur oxides (SO_x), ammonia, etc., to cause secondary aerosols, ozone, and photochemical smogs [2–4]. This reactivity poses significant threats to both ecosystems and public health. Among them, toluene finds extensive application in paints, adhesives, rubber, leather processing, making it a compound of high concern [5–7]. Given its toxicity and volatility, toluene has been included in the Pollutant Release and Transfer Register (PRTR) by many countries [8], and is often used as a model pollutant in VOCs eliminating research.

A range of methods, including adsorption, condensation, plasma degradation, membrane separation, biological oxidation, catalytic oxidation, and photocatalytic oxidation, have been explored for VOC elimination [3,9]. Among these, catalytic oxidation is widely regarded as one of the most viable routes for toluene abatement due to its high treatment efficiency, low energy requirements, ease of operation, and limited byproduct formation [10,11]. Consequently, the development of catalysts that exhibit high activity, robust stability, low cost, and green attributes remains a central research priority.

It is well known that precious metal catalysts are widely used for catalytic oxidation of VOCs due to their superior catalytic activity, good water-resistance and stability [12]. Palladium (Pd)-based catalysts with the remarkable capability in activating carbon-hydrogen (C-H) bonds can better adsorb and activate reactants, which makes them the preferred choice for practical applications [6,13–15]. Furthermore, considerable research has focused on the strong metal-support interaction (SMSI) in supported noble metal catalysts. This phenomenon markedly promotes catalytic oxidation through the construction of metal-oxide interfaces and the modification of charge transfer pathways [16]. The SMSI effect and the resulting catalytic performance were additionally correlated with the low metal-oxygen bond energy at the metal-support interface [17]. Wu et al. [10] synthesized serial Pd/TiO_2 catalysts with tailored surface structures—including Pd speciation, Ti^{3+}/oxygen defect density, and $Pd\text{-}TiO_2$ interactions—via various synthetic routes. A key finding was that the toluene oxidation conversion was remarkably improved at the interfaces formed between Pd nanoparticles and the mesoporous TiO_2 framework. This phenomenon has also been observed for Pd supported on reducible metal oxides, particularly in the case of Pd/CeO_2, due to facile charge transfer at the metal-support interface [18]. These findings underscore that the interfacial interaction between metals and oxide supports is critical for toluene oxidation, offering valuable guidance for future catalyst design.

However, under special condition such as steel refining, coal burning, power plants, and vehicle, SO_2 is often an inevitable component in exhaust gas [16,19,20]. The highly electronegative SO_2 can interact with the d-orbitals of precious metals causing the electrons of the precious metals moving toward SO_2, thus hindering the adsorption and activation of pollutants [12]. SO_2 can also weaken the interaction between the precious metal and the carrier, leading to the aggregation of precious metal particles, thereby reducing the catalyst activity. Furthermore, the rearrangement of the crystal structure can be induced due to the interaction between SO_2 and precious metals. It is reported that the adsorption of SO_2 results in the recrystallization of Pt (111) into Pt (100) driven through surface diffusion, thereby reducing the surface free energy [16]. Additionally, SO_2 will react with the support and form sulfates during the catalytic oxidation reactions, which cover the surface active sites and damage the catalyst structure, resulting in poisoning and deactivation of catalysts [19,21]. However, the analysis of the sulfur poisoning mechanism and sulfur-resistant catalyst design is not comprehensive due to the limited types of catalysts.

Different combinations of supports and precious metals exhibit varying effects. Besides, the sulfur poisoning process involves the formation, migration and stability of sulfur is widely considered to be influenced by the properties of supports [12]. For instance, Payan et al. [22] reported that the support played a critical role in acetone decomposition, influencing the process both microscopically–by altering the oxidation state of silver–and macroscopically–by governing the dominant oxidation mechanism. Under these effects, $Ag@CeO_2$ operated primarily via ozone-assisted photocatalytic oxidation, whereas $Ag@Al_2O_3$ and Ag@ZSM-5 followed a catalytic ozonation pathway [23]. Escandon et al. [24] compared the effects of four different Pd catalysts (with Al_2O_3, SiO_2, ZrO_2 and TiO_2 as carriers) on the SO_2 poisoning during the methane oxidation process. The Pd/SiO_2 catalyst rapidly lost its activity because the highly acidic SiO_2 could not be sulfated, causing the sulfur species to quickly occupy the Pd sites on the catalyst surface and thus generating $PdSO_4$ with low catalytic activity of $PdSO_4$. However, the other carriers (Al_2O_3, ZrO_2 and TiO_2) could receive the sulfur species produced at the Pd sites, thereby alleviating the poisoning of the precious metal sites. Due to the stronger acidity, the sulfates formed on TiO_2 and ZrO_2 are less thermally stable than those formed on Al_2O_3. Besides, some carriers with large oxygen storage capacity or active oxygen species including CeO_2, MnO_2, Co_3O_4, etc., are more likely to combine with SO_2 to form sulfuric acid salts with higher thermal stability [12,16,21]. Interestingly, for catalysts with Al_2O_3, TiO_2, ZrO_2 and CeO_2 as carriers, the addition of SO_2 has a promoting effect on the conversion of certain gaseous pollutants, while the catalysts with un-sulfided SiO_2 carriers do not show a similar promotional effect [12,25]. The promoting effect of SO_2 stems from the changes in the performance of the catalyst, which in turn influences the degradation mechanism of pollutants. Clarifying the mechanism of sulfur poisoning can lay the foundation for the design and regeneration of sulfur-resistant catalysts. To date, limited attention has been paid to the sulfur resistance of supported Pd catalysts during the catalytic oxidation of toluene.

Herein, a panel of supported Pd catalysts (with CeO_2, TiO_2, Al_2O_3, and SiO_2 as the support) was fabricated and systematically evaluated for toluene oxidation, with a focus on both catalytic activity and sulfur resistance. Subsequently, a combination of characterization tools–XRD, H_2-TPR, NH_3-TPD, FT-IR, TG, and XPS–was utilized to unravel the support-dependent sulfur resistance mechanisms.

2. Experimental Section

2.1. Catalysts Preparation

2.1.1. Preparation of Pd-Based Catalysts with Different Carriers

Four supported Pd catalysts, namely Pd/TiO_2, Pd/SiO_2, Pd/Al_2O_3, and Pd/CeO_2, were prepared for this study. Commercial anatase TiO_2 (99.8%, Aladdin), SiO_2 (99.8%, Aladdin), γ-Al_2O_3 (99.99%, Aladdin) and $Ce(NO_3)_3 \cdot 6H_2O$ (99.99%, Aladdin) were thermally decomposed at 500 °C for 4 h with a ramp rate of 5 °C·min^{-1} to obtain TiO_2, SiO_2, γ-Al_2O_3 and CeO_2 supports.

Incipient wetness impregnation was employed to prepare supported catalysts targeting a nominal Pd loading of 0.5 wt%. For each sample, 1.9155 g of the support was first dispersed into an aqueous solution, then slowly added 3 mL of $Pd(NO_3)_2$ solution (0.03 mol·L^{-1}), and stirred with a magnetic stirrer at room temperature for 3 h. Subsequently, they were placed in a water bath at 80 °C for evaporation and then dried in a 110 °C oven for 4 h. Finally, four supported Pd catalysts were obtained by calcining for 6 h in the muffle oven at 400 °C with a heating rate of 5 °C·min^{-1}.

2.1.2. Pretreatment of Sulfur Poisoning Catalysts

All synthesized catalysts were pretreated in a fixed-bed quartz tubular reactor with 1000 ppm SO_2/N_2 at 300 °C for 2 h. Prior to this, 0.6 g of Pd-based catalyst was heated from room temperature to 300 °C at a heating rate of 5 °C·min^{-1} in an air atmosphere. The flow rate of air and 1.0 vol% SO_2/N_2 were respectively set at 180 mL·min^{-1} and 20 mL·min^{-1}. The final obtained samples were denoted as Pd/TiO_2-S, Pd/SiO_2-S, Pd/Al_2O_3-S, and Pd/CeO_2-S.

2.2. Catalysts Characterization

Inductively coupled plasma atomic emission spectrometer (ICP-AES) produced by Thermo Fisher Scientific (Waltham, MA, USA) was used to determine the Pd elemental content of the calcined catalysts.

The X-ray diffraction (XRD) analysis was performed on a Philips X 'Pert Pro Diffractometer (Malvern Panalytical, Almelo, The Netherlands) using Cu Kα radiation (λ = 0.15408 nm). Diffraction patterns were recorded in the 2θ range of 10–80° at a scanning rate of 10°·min^{-1} with a step size of 0.02°.

An ASAP 2020 specific surface area analyzer (Micromeritics, Norcross, GA, USA) was employed to evaluate the specific surface areas (S_{BET}) of the catalysts based on N_2 adsorption isotherms obtaining at −196 °C. Before analysis, each sample was subjected to vacuum pretreatment at 300 °C for 4 h.

Thermogravimetric analysis (TGA) measurements was conducted on a Netzsch STA 449C analyzer (Netzsch, Selb, Germany), with the sample heated from 25 to 1000 °C at 10 °C·min^{-1} under a nitrogen atmosphere (40 mL·min^{-1}).

Raman measurements were performed on a LabRAM Aramis laser Raman spectrometer (Horiba Company, Kyoto, Japan) with a 532 nm Ar^+ laser excitation source, and spectra were acquired from 200 to 2000 cm^{-1}.

X-ray photoelectron spectra (XPS) analysis was carried out on a PHI 5000 VersaProbe X-ray photoelectron spectrometer (PHI Corporation, Kanagawa, Japan) equipped with an Al Kα X-ray source (1486.68 eV, 15 kW) at an ultrahigh vacuum of 8×10^{-10} Pa. The obtained spectra were processed using Avantage software, with binding energies (BE) referenced to the adventitious C 1s signal at 284.8 eV to account for charging effects.

Fourier transform infrared (FTIR) spectra were obtained using a Nicolet IS-50 FT-IR (Thermo scientific, Waltham, MA, USA) in attenuated total reflection (ATR) configuration with a diamond prism. The spectra were acquired in a frequency region of 4000–500 cm^{-1} with a resolution of 4 cm^{-1}. All spectra were recorded over the range of 4000–500 cm^{-1} at a resolution of 4 cm^{-1}.

The temperature-programmed desorption of ammonia (NH_3-TPD) was performed using a Nicolet IS10 FT-IR spectrometer (Thermo Scientific, Waltham, MA, USA) to evaluate the acid property of catalysts. Each sample (100 mg) was first pretreated in Ar (100 mL/min) at 300 °C for 1 h and cooled to room temperature. Adsorption was carried out by exposing the sample to 500 ppm NH_3/Ar (100 mL/min) for 1 h, followed by Ar purging (100 mL/min) to remove physisorbed NH_3. The desorption profile was then obtained by heating from 30 to 600 °C at 10 °C/min under Ar flow (100 mL/min).

Temperature-programmed reduction by hydrogen (H_2-TPR) was employed to assess catalyst reducibility. Each sample (20 mg) was first pretreated in the N_2 stream (40 mL/min) at 200 °C for 1 h, followed by cooling to room temperature. Upon achieving a stable baseline under 7.03 vol% H_2/Ar, the reduction profile was acquired by heating the sample to 850 °C at a constant rate of 10 °C/min.

2.3. Catalyst Activity Measurement

Toluene oxidation activities for as-prepared catalyst were evaluated in a continuous-flow fixed-bed microreactor. For each test, 100 mg of catalyst (20–40 mesh) was placed in a quartz tube and heated to 100 °C under a pure air flow (20% vol. O_2/N_2, total flow rate = 50 mL·min^{-1}). Subsequently, 1000 ppm toluene was introduced into the gas stream, and the reaction was conducted at a weight hourly space velocity (WHSV) of 30,000 mL·g^{-1}·h^{-1}. At each temperature step, the system was maintained for 30 min to achieve steady state, after which the products were analyzed by gas chromatography (GC-7920) equipped with flame ionization detector (FID) and thermal conductivity detector (TCD). Each reported value is the average of three replicate measurements. For water vapor tolerance tests, 5 vol% H_2O was introduced into the feed using a water saturator.

The conversion of toluene (X_{toluene}, %) was calculated using the following equation:

$$X_{\text{toluene}}\ (\%) = \left(1 - \frac{c_x}{c_0}\right) \times 100\% \tag{1}$$

where C_0 and C_x are the toluene concentration (ppm) in the inlet and outlet flow, respectively.

The carbon dioxide yield (Y_{CO_2}, %) and the selectivity of carbon dioxide production (S_{CO_2}, %) were calculated using the following equation:

$$Y_{\text{CO}_2}\ (\%) = \frac{c_{\text{co}_2}}{7 \times c_0} \times 100\% \tag{2}$$

$$S_{\text{CO}_2}(\%) = \frac{Y_{\text{co}_2}}{X_{\text{toluene}}} \tag{3}$$

where C_{CO_2} is the CO_2 concentration (ppm) in the outlet flow.

Within the temperature range where the conversion rate of the catalyst for toluene was less than 20%, the activation energy (*Ea*) of the catalyst was calculated using the Arrhenius formula. The calculation formula is as follows:

$$\ln k = \ln A - \frac{Ea}{RT} \tag{4}$$

where k denotes the reaction rate (mol·s^{-1}); *Ea* represents the apparent activation energy (kJ·mol^{-1}); and A is the pre-exponential factor.

3. Results and Discussion

3.1. Catalytic Performance for Toluene Combustion

As shown in Figure 1a, the toluene combustion activity of four Pd catalysts with different supports was evaluated before and after SO_2 pretreatment. The results revealed a strong dependence of catalytic performance on the carrier material. Noticeably, despite similar nominal Pd loadings (0.45~0.49 wt%, Table S1), the catalysts displayed markedly different oxidation activities, likely arising from the varying degrees of synergistic interaction between Pd and each support. As for fresh catalysts, the activity was in the following order: Pd/CeO_2 > Pd/Al_2O_3 > Pd/SiO_2> Pd/TiO_2. As listed in Table 1, Pd/CeO_2 catalyst reached a T_{90} value of 220 °C for toluene conversion, superior to that of the MOF-based catalyst (6% CeO_2@MIL-101(Fe)), which exhibited a T_{90} of 239 °C [26]. In additon, the CO_2 selectivity at T_{90} remained above 98% for all catalysts, confirming complete oxidation of toluene to CO_2 without significant byproduct formation.

Figure 1b exhibits the Arrhenius plots for the oxidation of toluene over fresh catalysts. It can be clearly observed that the Ea of each catalyst follows the following rules: Pd/CeO_2 (38.44 kJ·mol^{-1}) < Pd/Al_2O_3 (48.45 kJ·mol^{-1}) < Pd/SiO_2 (50.89 kJ·mol^{-1}) < Pd/TiO_2 (55.71 kJ·mol^{-1}). This is in agreement with the sequence of reactivity. For instance, the Pd/CeO_2 sample has the lowest Ea value, indicating that it has the lowest potential barrier in the catalytic oxidation of toluene and therefore exhibits superior low-temperature activity.

After SO_2-pretreated, the catalysts showed differing levels of activity suppression, whereas Pd/TiO_2 remained the most active (Figure 1a). As shown in Table 1, the Pd/CeO_2-S catalyst exhibited the most pronounced decline in activity, with its T_{90} value increasing sharply from 220 °C to 294 °C. This was followed by the Pd/Al_2O_3-S and Pd/SiO_2-S catalysts, whose T_{90} values rose by 27 °C and 36 °C, respectively. It is worth noting that the Pd/Al_2O_3-S catalyst in the present study achieved a T_{90} of 260 °C for toluene oxidation, considerably outperforming the sulfur-poisoned catalysts reported in previous studies. Specifically, Wang et al. [27] reported a T_{90} of 370 °C for a MnO_2/γ-Al_2O_3-S catalyst during toluene combustion, while Jiang et al. [21] observed a T_{90} of 400 °C for a Co_3O_4/γ-Al_2O_3-S catalyst containing a spinel structure. Additionally, the Ea value of Pd/CeO_2-S increased

remarkedly (from 38.44 to 51.23 kJ/mol), whereas that of Pd/TiO_2-S increased only slightly (from 55.71 to 58.31 kJ/mol), indicating that TiO_2 exhibits higher sulfur tolerance. Thus, the different sulfur resistance of catalysts may be attributed to the inherent characteristics of the carriers.

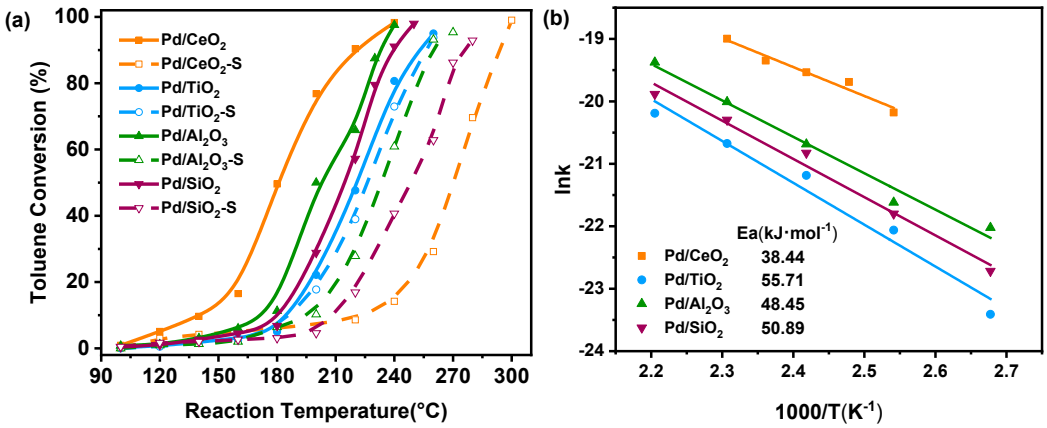

Figure 1. (**a**) Conversion of toluene over fresh and SO_2 pretreated samples; (**b**) Arrhenius plots for the oxidation of toluene over fresh samples.

Table 1. Kinetic parameters of fresh and sulfur-poisoned catalysts for toluene oxidation.

Sample	T_{50} (°C)	T_{90} (°C)	ΔT_{90} (°C)	CO_2 selectivity at T_{90} (%)	Ea (kJ·mol^{-1})
Pd/CeO_2	180.3 ± 2.0	219.4 ± 2.0	-	99.2 ± 0.3	38.44
Pd/CeO_2-S	270.3 ± 2.0	293.9 ± 2.0	74.5 ± 3.0	98.4 ± 0.5	51.23
Pd/TiO_2	221.4 ± 2.0	253.0 ± 2.0	-	98.7 ± 0.4	55.71
Pd/TiO_2-S	226.5 ± 2.0	256.4 ± 2.0	3.4 ± 2.0	98.2 ± 0.4	58.31
Pd/Al_2O_3	200.0 ± 2.0	232.5 ± 2.0	-	98.9 ± 0.3	48.45
Pd/Al_2O_3-S	233.4 ± 2.0	258.0 ± 2.0	25.5 ± 3.0	98.1 ± 0.6	54.49
Pd/SiO_2	214.9 ± 2.0	239.1 ± 2.0	-	98.5 ± 0.5	50.89
Pd/SiO_2-S	248.4 ± 2.0	275.7 ± 2.0	36.6 ± 3.0	98.0 ± 0.6	59.19

Note: ΔT_{90} = T_{90} (poisoned sample) − T_{90} (fresh sample). Negative values indicate decreased T_{90} (activation); positive values indicate increased T_{90} (deactivation).

3.2. Structural Characterization of Catalysts

To elucidate the impact of SO_2 pretreatment, the structural properties of the catalysts were thoroughly examined. The XRD patterns of both fresh and spent catalysts are presented in Figure 2. CeO_2 (JCPDS PDF# 34-0394), anatase TiO_2 (JCPDS PDF# 21-1272), and γ-Al_2O_3 (JCPDS PDF# 2-1420) can be found in Pd/CeO_2, Pd/TiO_2, Pd/Al_2O_3, respectively [28–30]. A broad diffraction peak observed at approximately 2θ = 22.6° is indexed to the (101) plane of SiO_2 (JCPDS PDF# 82-1557) [31]. The absence of discernible Pd diffraction peaks in all catalysts suggested the presence of highly dispersed Pd species. No significant changes were observed in the XRD spectra of the sulfur poisoning catalysts, indicating that the SO_2 pretreatment did not cause any damage to the crystal structure of the samples. From this, it can be concluded that crystal pattern is not the decisive factor influencing the sulfur resistance of each catalyst. Meanwhile, no signal of sulfates were observed, which might be due to the insufficient amount of sulfate species formed or the particle size being too small to detect [16].

N_2 adsorption-desorption tests were further conducted to explore the structural variation after SO_2 pretreatment. Table 2 and Figure S1 presented the textural properties of Pd/CeO_2, Pd/Al_2O_3, Pd/SiO_2, and Pd/TiO_2, including BET surface area (70.0, 67.0, 137.4, and 141.1 $m^2 \cdot g^{-1}$) and average pore diameter (12.9, 18.1, 18.4, and 24.3 nm). Combining with the activity patterns, it was found that although the specific surface area of Pd/Al_2O_3 and Pd/SiO_2 catalysts was almost twice that of Pd/CeO_2 and Pd/TiO_2, their catalytic performance for toluene was still inferior to Pd/CeO_2 and slightly better than that of Pd/TiO_2. Therefore, increasing the specific surface area of the carrier can help promote the catalytic performance for toluene oxidation, but it is not a determining factor. As

shown in Figure S1, typical IV-type isothermal lines were observed on Pd/CeO_2, Pd/Al_2O_3, Pd/SiO_2, Pd/TiO_2, and each of them had a hysteresis loop of H3. This indicates that all catalysts had mesoporous structures originating from the piling of the particles [32].

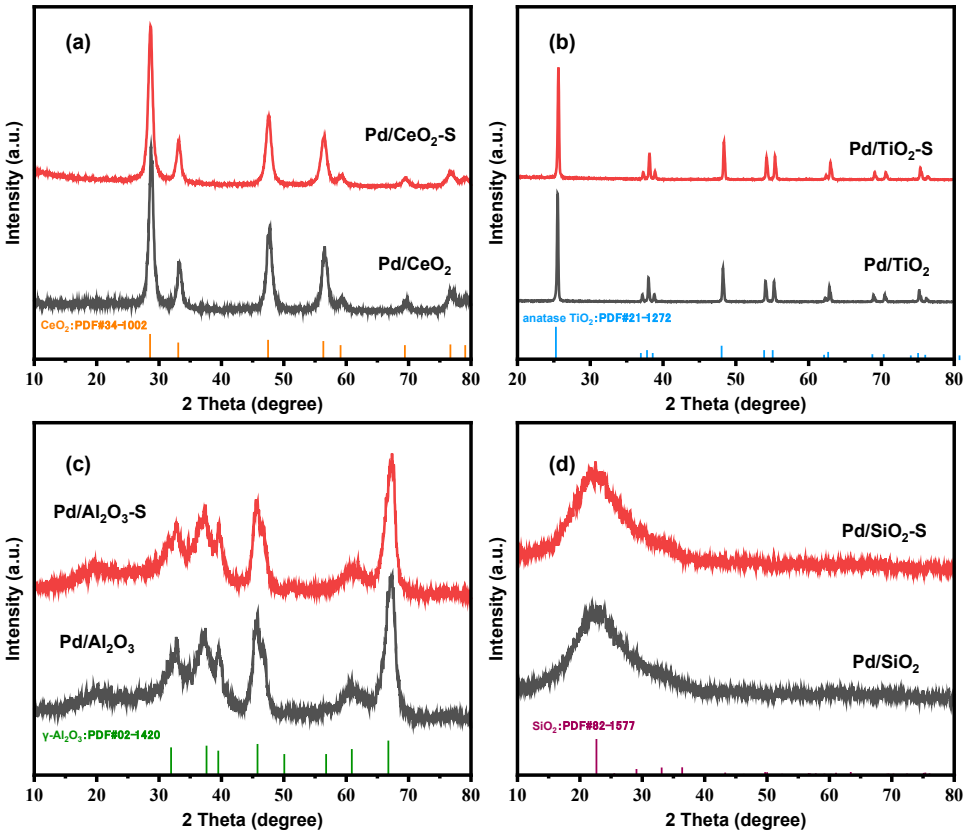

Figure 2. XRD patterns of different samples of fresh and SO_2 pretreated samples: (**a**) Pd/CeO_2; (**b**) Pd/TiO_2; (**c**) Pd/Al_2O_3; (**d**) Pd/SiO_2.

Table 2. BET results of fresh and SO_2 pretreated samples.

Sample	Surface Area ($m^2 \cdot g^{-1}$)	Pore Volume ($cm^3 \cdot g^{-1}$)	Average Diameter (nm)
Pd/CeO_2	70.0	0.23	12.9
Pd/CeO_2-S	48.7	0.19	15.8
Pd/TiO_2	67.0	0.30	18.1
Pd/TiO_2-S	62.4	0.28	17.7
Pd/Al_2O_3	137.4	0.73	21.6
Pd/Al_2O_3-S	134.3	0.63	18.4
Pd/SiO_2	141.1	0.85	24.3
Pd/SiO_2-S	138.4	0.68	19.9

The specific surface area for sulfur-impacted catalysts all showed a decreasing trend. Among them, the S_{BET} of Pd/CeO_2-S decreased from 70.0 to 48.7 $m^2 \cdot g^{-1}$, with the most significant drop. This might be due to the formation of sulfates that clogged some of micropores [33]. The samples of Pd/Al_2O_3 and Pd/SiO_2 with rather large specific surface areas exhibited no significant change after SO_2 pretreatment, mainly because the amount of sulfate produced during the sulfidation process was relatively small. This is consistent with the findings of Bazin et al. [32], who demonstrated that the formation rate and extent of sulfate was directly linked to the specific surface area of the sample. It is worth noting that, even though the Pd/TiO_2 sample had a specific surface area comparable to that of Pd/CeO_2, it did not change significantly after sulfidation. This indicated chemistry of support dominates more than surface area. Therefore, it can be inferred that the specific surface area was not the primary factor

governing the catalytic performance for toluene oxidation; instead, the chemical properties of the support (such as its acidity/basicity, redox properties, and sulfation affinity) played a dominant role.

3.3. Surface Sulfate Species of the Catalysts

FT-IR was performed to determine the surface functional groups variation and the formation of sulfate species on the deactivated catalysts. As shown in Figure 3, all the samples exhibited peaks corresponding to the stretching/deformation vibration of surface hydroxyl groups (O-H) at 3700–3200 and 1650–1620 cm^{-1} [34]. Furthermore, in the Pd/CeO_2 sample, there were still stretching vibration peaks of Ce-O bonds at 1040 and 565 cm^{-1} [35]; in the Pd/Al_2O_3 sample, the peaks near 810 and 545 cm^{-1} belonged to the vibration of Al-O bonds [31]; in the Pd/SiO_2 sample, the inverted peaks at 1070 and 800 cm^{-1} characteristic of the symmetric stretching vibration of surface Si-O bonds and the antisymmetric Si-O-Si stretching vibration of SiO_x, respectively [36]. After pretreatment with SO_2, the type and intensities of the peaks for both sulfided support and sulfided Pd-based samples exhibited minimal changes (Figure S2), indicating that SO_2 primarily interacts with the support rather than directly bonding with the Pd sites. Notably, no peaks related to sulfates were observed in the Pd/SiO_2 sample, while weak sulfate peaks were detected in Pd/Al_2O_3 and Pd/TiO_2 samples. It is worth noting that a broad peak of double-chained sulfate anion (S=O symmetric stretching vibration) appeared significantly around 1120 cm^{-1} in the Pd/CeO_2 sample, as well as a corresponding shoulder peak of S-O asymmetric stretching vibration appeared at 1040 cm^{-1} [37]. Specifically, according to literature reports [27,38–40], the broad band formed at 1120 cm^{-1} after SO_2 poisoning, along with the decrease in the -OH stretching vibration at 3420 cm^{-1}, can be ascribed to the removal of surface water during SO_2 poisoning and the formation of an ionic sulfate structure. Therefore, it is proposed that SO_2 is adsorbed on the catalyst surface in the form of SO_4^{2-}. Besides, the ranking of the amount of sulfate species generated by the four catalysts during the sulfation process is: $Pd/CeO_2 > Pd/Al_2O_3 > Pd/TiO_2 > Pd/SiO_2$. From this, it can be seen that when CeO_2 is used as the carrier, the catalyst is very prone to adsorb SO_2 and produce sulfates, resulting in the occupation of the catalyst's active sites and subsequent deactivation. This is in agreement with the results of catalytic activity and the specific surface area variation.

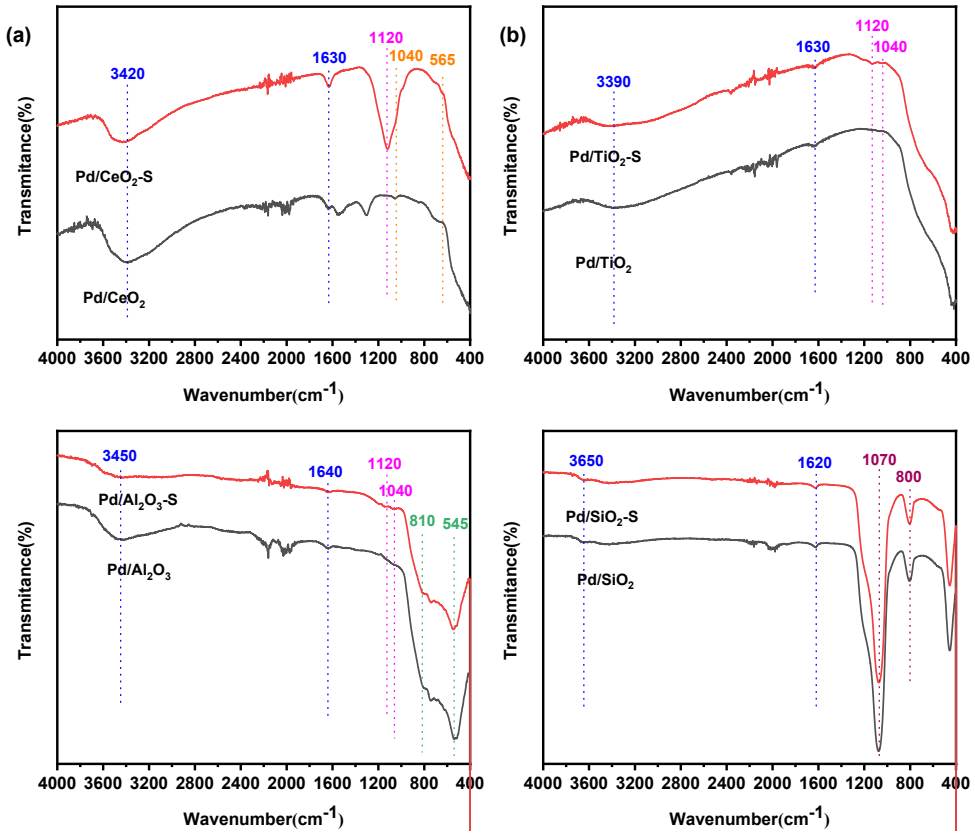

Figure 3. FT-IR patterns of fresh and SO_2 pretreated samples: (**a**) Pd/CeO_2; (**b**) Pd/TiO_2; (**c**) Pd/Al_2O_3; (**d**) Pd/SiO_2.

The amount of the sulfate formed on Pd/CeO_2-S, Pd/TiO_2-S, Pd/Al_2O_3-S, and Pd/SiO_2-S catalysts was further estimated from TG characterization and shown in Figure 4. It is well known that the weight loss observed in the 50–200 °C temperature range is due to the desorption of water and hydroxyl groups on the catalyst surface [16].

Hence, the weight loss observed at temperatures above 200 °C is likely to be related to the decomposition of sulfates. For $PdSO_4$, it can directly decompose to form the metal Pd at around 550 °C in an inert atmosphere such as He or N_2, while in an oxygen atmosphere, the decomposition of $PdSO_4$ does not occurred until 800 °C [41]. The thermogravimetric test in this experiment was conducted under N_2 atmosphere. Evidently, the Pd/CeO_2-S catalyst exhibited a sharp weight loss about 5% within the narrow temperature range of 600–750 °C, which was attributed to the decomposition of cerium sulfate ($Ce_2(SO_4)_3$). The weight loss about 2% occurred at 650 °C for Pd/Al_2O_3-S sample is attributed to the thermal decomposition of aluminium sulfate ($Al_2(SO_4)_3$), which is consistent with the reports in the literature [42]. In addition, the Pd/SiO_2-S sample has an additional weight loss of approximately 0.4% compared to the Pd/SiO_2 sample within the temperature range of 550–700 °C. Since the carrier SiO_2 is difficult to react with SO_2 to form sulfates, this was attributed to the decomposition of $PdSO_4$. Particularly, the Pd/TiO_2-S sample still exhibited a slow weight loss trend at a temperature of 200 °C, which might be related to the decomposition of titanium sulfate ($TiSO_4$). Studies have shown that $TiSO_4$ begins to decompose into titanium oxysulfate ($TiOSO_4$) at 150 °C, and from 300 to 500 °C, $TiOSO_4$ decomposes to form anatase TiO_2 [40]. Compared with the other three catalysts, the weight loss phenomenon of the Pd/TiO_2-S sample was less obvious. And the weight loss of the Pd/TiO_2-S sample in the 300–700 °C range originated from the decomposition of $TiSO_4$ and $PdSO_4$. Therefore, the Pd/CeO_2-S sample readily reacted with SO_2 to form a large amount of stable $Ce_2(SO_4)_3$ deposition, which may be the key factor contributing to the decline in its anti-sulfur performance; While the Pd/TiO_2 sample exhibited excellent sulfur resistance mainly due to the formation of a small amount of easily decomposable $TiSO_4$ and $PdSO_4$ on its surface. Additionally, the quantitative relationship between sulfate loading (TG mass loss, mmol·g^{-1}) and deactivation magnitude (ΔT_{90}, °C) have been analyzed, and the results are listed in Table S2. Notably, Pd/CeO_2 shows the greatest activity loss, whereas Pd/TiO_2 shows the least, suggesting that Pd/TiO_2 has high sulfur tolerance.

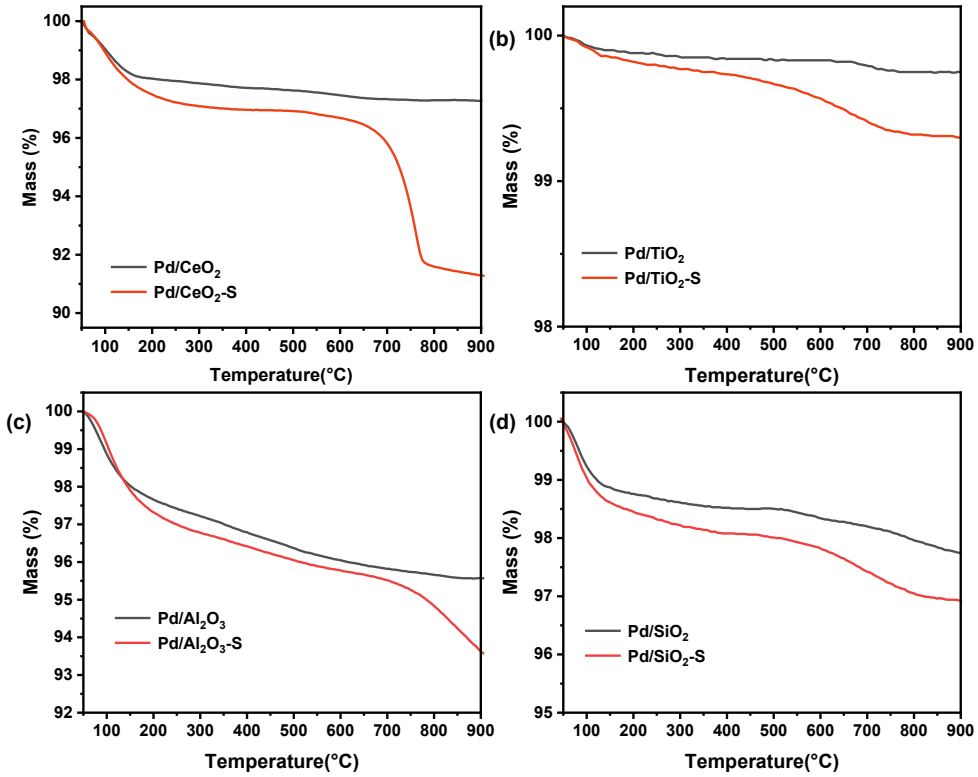

Figure 4. TG results of fresh and SO_2 pretreated samples: (**a**) Pd/CeO_2; (**b**) Pd/TiO_2; (**c**) Pd/Al_2O_3; (**d**) Pd/SiO_2.

3.4. Chemical States of the Catalysts

To elucidate the changes in surface species and chemical states, the samples were characterized by XPS. The Pd 3d XPS spectra of samples are shown in Figure 5. The peaks at binding energies of 334.8–335.5 eV and 340.4–341 eV were attributed to the Pd^0 $3d_{5/2}$ and $3d_{3/2}$ respectively, while peaks at binding energies of 336.5–337.2 eV and 341.8–342.4 eV were assigned to Pd^{2+} $3d_{5/2}$ and $3d_{3/2}$ [43]. For the fresh samples, except for Pd/TiO_2 which only contained the Pd^{2+} species, the other three catalysts have both oxidized and metallic forms of Pd. According to Table S3, the form of Pd^0 in Pd/CeO_2 sample accounted for 28.2% of the total Pd species, which was significantly higher than that in Pd/Al_2O_3 (12.9%) and Pd/SiO_2 (11.8%). The Pd^0/Pd_{total} ratios of the four samples

were consistent with their order of reactivity, which might be the reason why the Pd/CeO_2 sample exhibited excellent low-temperature catalytic activity. Because, numerous previous studies have reported that the metallic Pd is more favorable than Pd^{2+} for electron enrichment and enhanced electron-hole separation efficiency on the catalyst surface [44], and is usually regarded as an active site on the catalyst surface. After SO_2 pretreatment, the proportion of Pd^0 species in the samples all decreased. Among them, the Pd/CeO_2-S sample showed the largest decrease of 8.4%, indicating that the amount of Pd active component reacting with SO_2 to form $PdSO_4$ was the largest. This is consistent with the FT-IR and TG data. It is precisely because of the significant loss of the Pd^0 active component that the low-temperature activity of the Pd/CeO_2-S catalyst has dropped significantly [42]. Meanwhile, due to the influence of the formation of $PdSO_4$, the binding energy of Pd 3d in four samples shifted towards higher binding energy [19].

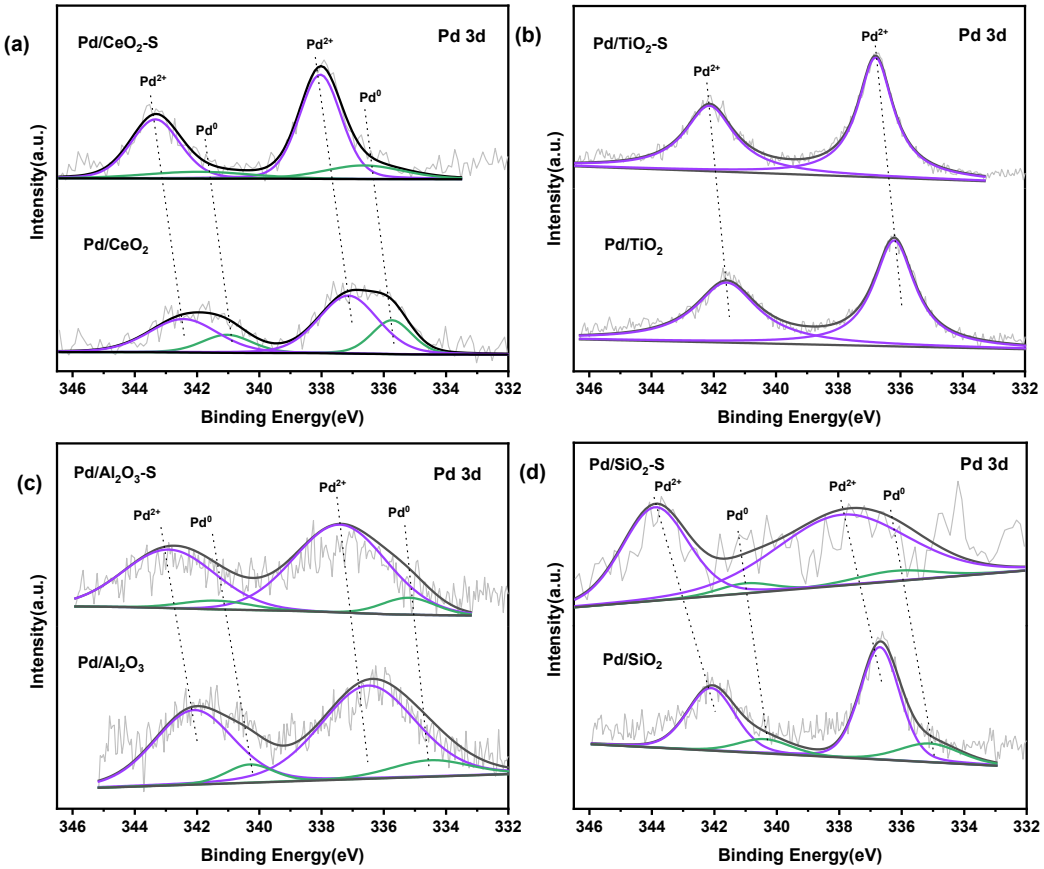

Figure 5. XPS spectra of Pd 3d for fresh and SO_2 pretreated samples: (**a**) Pd/CeO_2; (**b**) Pd/TiO_2; (**c**) Pd/Al_2O_3; (**d**) Pd/SiO_2.

XPS analysis of the O 1s region was conducted on catalysts with the results shown in Figure 6. For the Pd/CeO_2, Pd/TiO_2, and Pd/Al_2O_3 samples, three separate peaks, located at 529.6–530.0 eV, 530.9–531.8 eV, and 532.6–533.2 eV, were correspond to surface lattice oxygen (O_{latt}), surface adsorbed oxygen (O_{ads}), and adsorbed hydroxyl or water molecule oxygen (O_{-OH}) [4]. However, the Pd/SiO_2 sample exhibited the O 1s binding energy of SiO_2 [37], which might be due to the weak interaction between Pd and SiO_2, resulting in the absence of a strong chemical bond. As reported previously, surface adsorbed oxygen species is beneficial for the progress of redox reactions [5]. Table S3 showed that the Pd/CeO_2 sample contained a large amount of adsorbed oxygen species (11.5%), indicating its excellent redox capability, which is conducive to enhancing its toluene oxidation activity. After SO_2 pretreatment, the O_{ads} content in Pd/CeO_2-S, Pd/TiO_2-S, and Pd/Al_2O_3-S samples increased due to the formation of sulfates [45]. As is well known, CeO_2 has strong oxygen storage and release properties, which leads to the fact that even in the absence of oxygen, CeO_2 will undergo intense interaction with SO_2 to form sulfates [26]. Therefore, the Pd/CeO_2-S sample produced the largest amount of sulfate, resulting in the most significant increase in the proportion of O_{ads} and the poorest anti-sulfur performance.

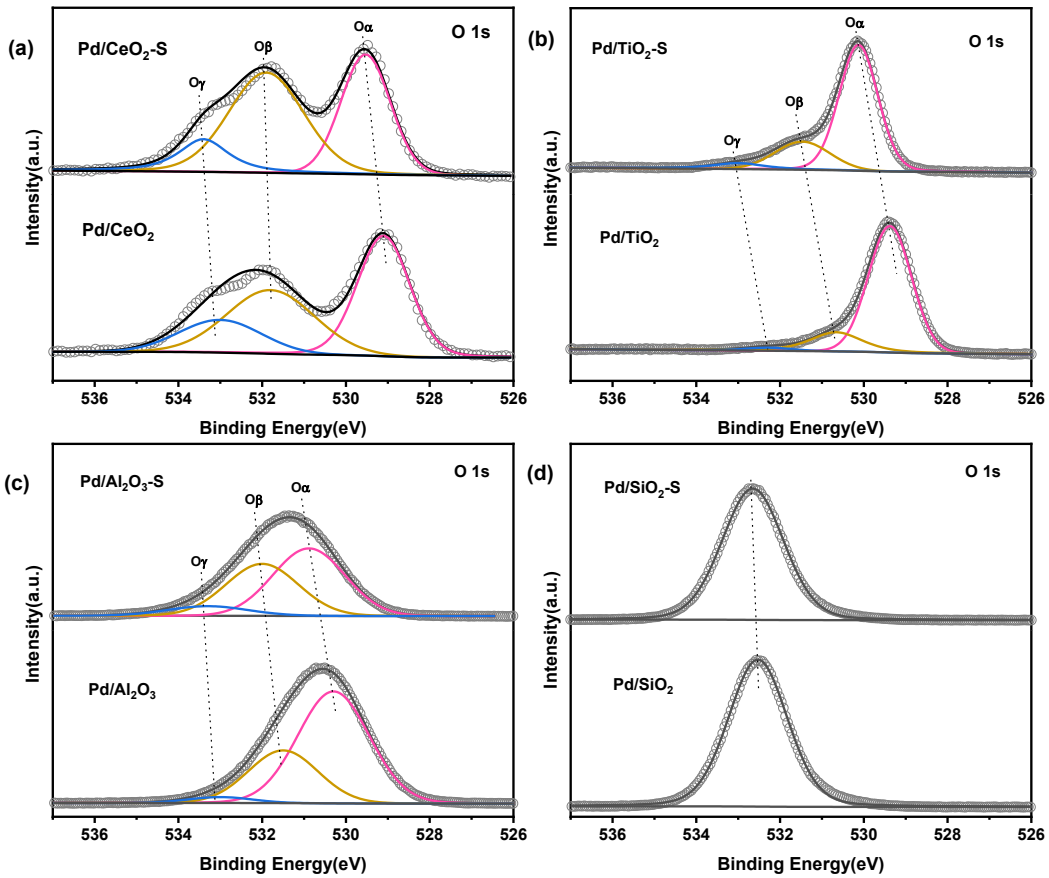

Figure 6. O 1s XPS spectra of fresh and SO_2 pretreated samples: (**a**) Pd/CeO_2; (**b**) Pd/TiO_2;(**c**) Pd/Al_2O_3; (**d**) Pd/SiO_2.

The S 2p XPS spectra of samples treated with SO_2 were shown in Figure S3. The characteristic peak with a binding energy of 169.1 eV was assigned to S^{6+} species, suggesting the formation of sulfate species [13]. Among them, the Pd/CeO_2-S sample exhibited the strongest peak intensity of the sulfate species, followed by the Pd/Al_2O_3-S, Pd/TiO_2-S and Pd/SiO_2-S samples. This is slightly inconsistent with the TG data. This might be due to the presence of a small amount of carrier sulfate ($TiSO_4$) in the Pd/TiO_2-S sample, while the Pd/SiO_2-S sample only has $PdSO_4$ species on its surface. Therefore, the weakest sulfate signal peak appeared on the surface of the Pd/SiO_2-S sample. Furthermore, it was found that the peak representing sulfate in the Pd/TiO_2-S sample shifted towards lower binding energy compared to the other three samples, indicating that the interaction between the surface sulfate and the catalyst was weaker, and it was more prone to decomposition.

3.5. Acidic Properties of Prepared Catalysts

The surface acidity of catalysts was investigated by NH_3-TPD with results shown in Figure 7. The NH_3-TPD curves of each sample were deconvoluted into three peaks (denoted as α, β and γ), centered at 50–200 °C, 200–350 °C and 350–450 °C, representing the weak, medium-strong, and strong acid sites, respectively [14]. Based on the quantitative analysis of NH_3-TPD (Table S4), the order of total acidity of four fresh samples is: Pd/Al_2O_3 (401 $\mu mol \cdot g^{-1}$) > Pd/SiO_2 (278 $\mu mol \cdot g^{-1}$) > Pd/CeO_2 (189 $\mu mol \cdot g^{-1}$) > Pd/TiO_2 (72 $\mu mol \cdot g^{-1}$). Byun et al. also found that the surface of the Pd/Al_2O_3 catalyst has abundant acidic sites [46]. However, the acid quantity pattern shown by NH_3-TPD was not significantly correlated with its catalytic activity. Therefore, the surface acidic sites are not the key factor influencing the catalytic oxidation performance of toluene. After SO_2 treatment, the acidity of all samples increased due to the formation of sulfates. The total NH_3 desorption amounts of the Pd/CeO_2-S and Pd/Al_2O_3-S samples increased by 547 and 598 $\mu mol \cdot g^{-1}$ respectively, which were significantly higher than 72 $\mu mol \cdot g^{-1}$ of Pd/TiO_2-S and 28 $\mu mol \cdot g^{-1}$ of Pd/TiO_2-S. It indicated that both the Pd/CeO_2 and Pd/Al_2O_3 samples have strong carrier adsorption capacity for sulfur, thus generating the most sulfate on the surface; while the Pd/TiO_2 sample has less sulfate deposition because the sulfate formed on the carrier surface is not stable, and the total desorption amount of NH_3 increased less. SiO_2 does not react with SO_2. The enhancement of surface acidity in Pd/SiO_2-S may all be attributed to the contribution of the noble metal sulfate ($PdSO_4$), resulting in the lowest increase in acidity. This is consistent with the previous S 2p XPS results. Likewise, the variations in acidity observed by NH_3-

TPD exhibited no strong correlation with the sulfur stability of the catalysts, suggesting that the surface acidic sites are not the key factor affecting the catalyst's anti-sulfur performance.

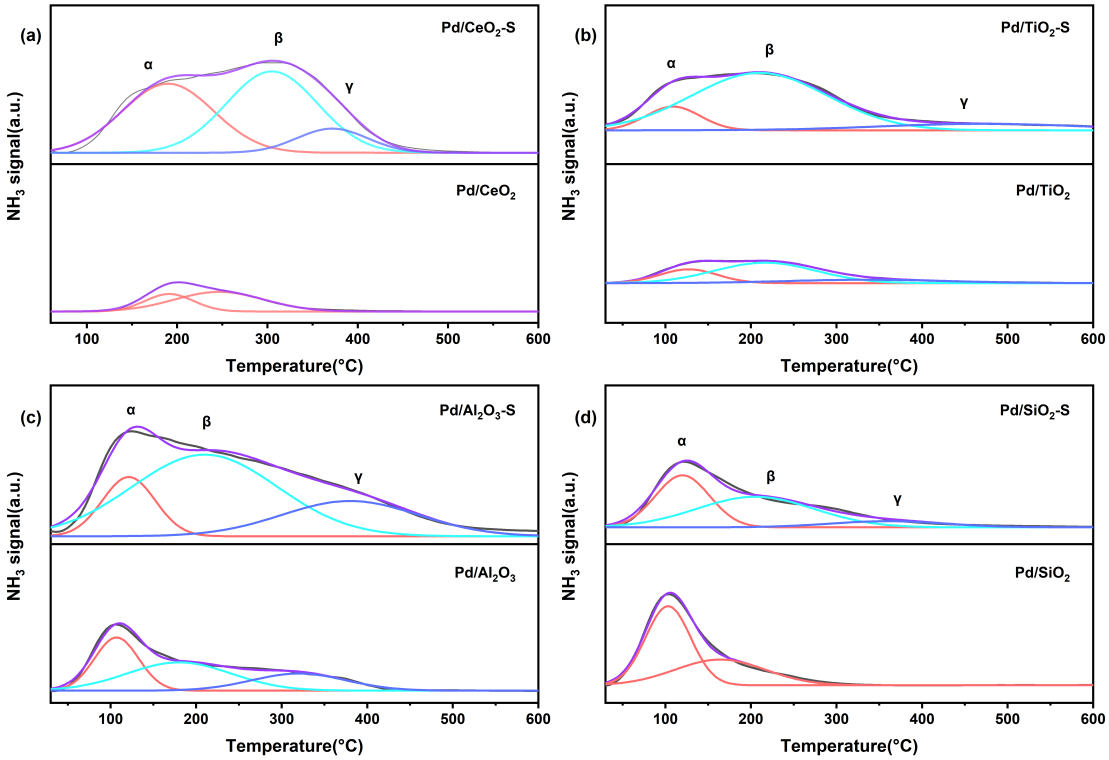

Figure 7. NH_3-TPD curves of different samples of fresh and SO_2 pretreated samples: (**a**) Pd/CeO_2; (**b**) Pd/TiO_2; (**c**) Pd/Al_2O_3; (**d**) Pd/SiO_2.

3.6. Redox Property of the Prepared Catalysts

H_2-TPR profiling was employed to compare the redox properties of the samples before and after SO_2 pretreatment, and the results were displayed in Figure 8. The TPR curves of Pd/CeO_2 at low temperatures appeared reduction peaks corresponding to the surface PdO species and the surface capping oxygen [47]. In the TPR curve of Pd/Al_2O_3, the signal appearing near 60 °C can be assigned to the reduction of surface Pd-O species. In contrast, negative peaks were observed at around 70 °C for Pd/TiO_2 and Pd/SiO_2 samples, which was due to the formation of β-PdH_x when H_2 hydrogenated PdO at room temperature [48]. In a reducing atmosphere, $PdSO_4$ will gradually decompose into different Pd_xS phases. Among them, PdS species were formed within the temperature range of 300–400 °C, while Pd_4S species were formed at 500–700 °C [20].

As seen in the figure, the TPR curves of each sample after SO_2 treatment all showed differences, with the most significant variations occurring in Pd/CeO_2-S and Pd/Al_2O_3-S. The disappearance of the low-temperature reduction peak of Pd/CeO_2-S indicated a significant decline in its redox performance [16]. Additionally, a reduction peak attributed to $PdSO_4$ and $Ce_2(SO_4)_3$ species appeared at 495 °C, suggesting that a large amount of $Ce_2(SO_4)_3$ was deposited on the surface of Pd/CeO_2-S sample [45]. Compared with the Pd/Al_2O_3 sample, the temperature of the low-temperature reduction peak of the Pd/Al_2O_3-S sample increased, which might be due to the sulfur poisoning of some surface PdO species, resulting in the formation of $PdSO_4$. Additionally, reduction peaks belonging to sulfates ($PdSO_4$ and $Al_2(SO_4)_3$) appeared within the range of 400–500 °C [12]. The reduction peak observed in the Pd/SiO_2-S sample at 610 °C is attributed to the decomposition of $PdSO_4$. While the Pd/TiO_2-S sample exhibited a weak reduction peak near 315 °C and 545 °C, which might respectively correspond to the reduction of trace $TiSO_4$ and $PdSO_4$. In summary, the redox properties of the catalyst are regarded as an important factor determining its sulfur resistance.

To elucidate the key factor governing catalyst deactivation, quantitative relationships between ΔT_{90} and three properties—sulfate loading, sulfate peak area, and total acid increment—were established using linear regression (Figure S4a–c). Sulfate loading (R^2 = 0.8861) and sulfate peak area (R^2 = 0.7429) showed strong positive correlations with ΔT_{90}, whereas total acid increment exhibited a weak correlation (R^2 = 0.2570). The consistent trend across all catalysts is visually confirmed in Figure S4d. Overall, these results indicated that sulfate accumulation was the dominant cause of deactivation in Pd-based catalysts, with increased surface acidity being

a secondary effect accompanying sulfate formation. A schematic overview of the structure–property–performance interplay for the Pd/CeO_2 and Pd/TiO_2 catalysts under SO_2 exposure was provided in Scheme 1.

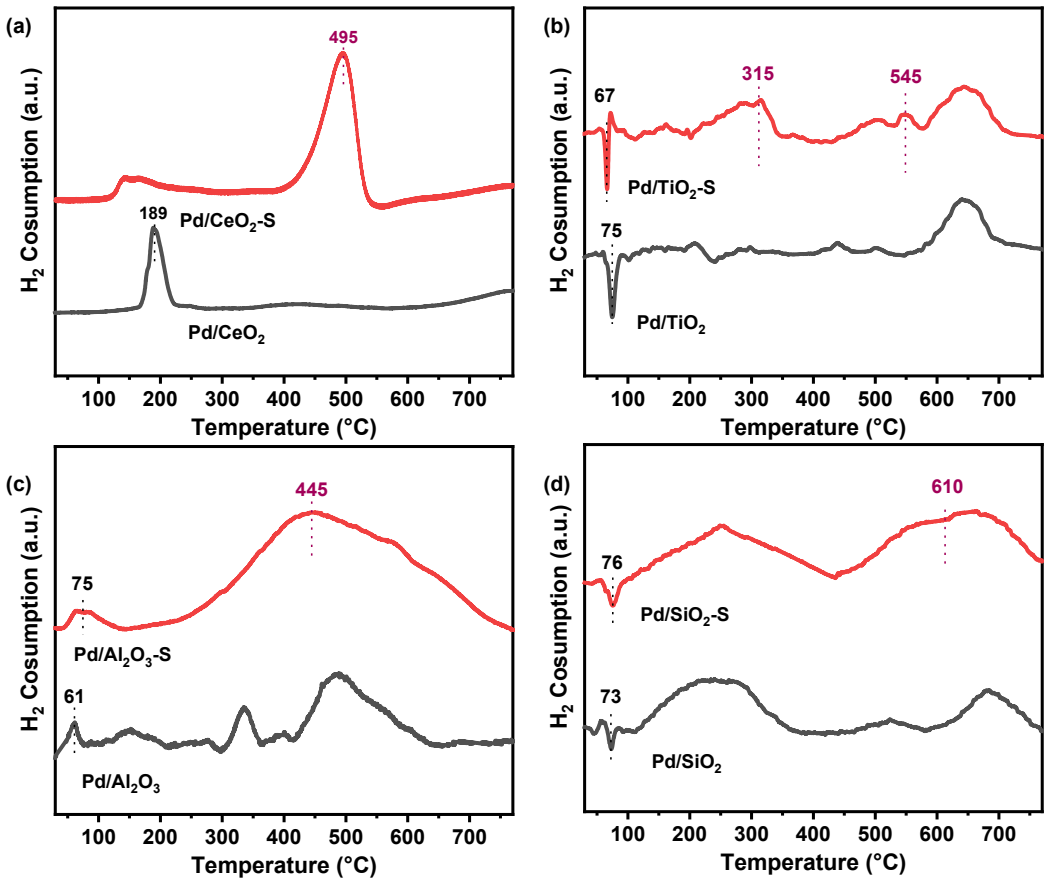

Figure 8. H_2-TPR curves of fresh and SO_2 pretreated samples: (**a**) Pd/CeO_2; (**b**) Pd/TiO_2; (**c**) Pd/Al_2O_3; (**d**) Pd/SiO_2.

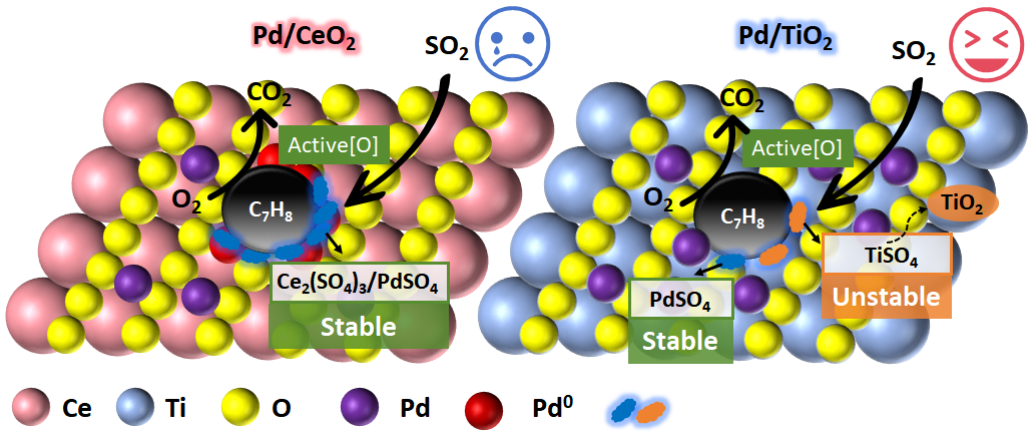

Scheme 1. The structure–property–performance correlations for Pd/CeO_2-S and Pd/TiO_2-S catalysts toward the toluene oxidation.

4. Conclusions

In this study, four Pd-based catalysts (Pd/CeO_2, Pd/Al_2O_3, Pd/TiO_2, and Pd/SiO_2) containing comparable nominal Pd loadings were synthesized using the incipient wetness impregnation. These catalysts exhibited markedly different performance in toluene combustion and sulfur resistance, with the oxidation activity ranking as Pd/CeO_2 > Pd/Al_2O_3 > Pd/SiO_2> Pd/TiO_2. Based on a series of characterizations, the higher content of Pd^0 and reactive oxygen species enable the Pd/CeO_2 sample to have more active sites and redox capabilities, which determines its optimal catalytic activity for toluene oxidation. However, their sulfur-tolerant performance does not follow the same trend as catalytic activity; instead, it seemed to correlate strongly with whether the support underwent

sulfation. For the Pd/CeO_2 catalyst, due to the strong adsorption ability of CeO_2 for SO_2, a large amount of stable sulfate deposits on the catalyst surface, blocking the internal pores and causing significant changes in its structural properties, ultimately leading to the poor sulfur resistance. On the contrary, the sulfate salts formed by the reaction of Pd/TiO_2 with SO_2 are unstable and prone to decomposition, which reduces the deposition of sulfate salts on the surface, thereby protecting the activity of the catalyst and presenting an excellent anti-sulfur performance.

Supplementary Materials

The additional data and information can be downloaded at: https://media.sciltp.com/articles/others/26042116 48219073/ESG-26020001-SM-FC-done.pdf. Figure S1: The N_2 adsorption-desorption isotherms and pore size distribution curves of samples: (a) and (c) fresh samples; (b) and (d) SO_2 pretreated samples. Figure S2: Comparison of the poisoning supports (CeO_2-S, TiO_2-S) and Pd-loaded samples (Pd/CeO_2-S, Pd/TiO_2-S). Figure S3: S 2p XPS spectra of the SO_2 pretreated samples. Figure S4: (a–c) Linear correlations between deactivation index ΔT_{90} and (a) total acid increment; (b) sulfate peak area; (c) sulfate loading for sulfated Pd-based catalysts; (d) Comparative performance of four catalysts, confirming sulfate accumulation as the primary deactivation driver. Table S1: The actual Pd contents in fresh samples. Table S2: Sulfate loading and normalized activity loss of sulfur-poisoned Pd-based catalysts with different supports. Table S3: The XPS data of all as-prepared samples. Table S4: The quantitative analysis results of NH_3-TPD of fresh and SO_2 pretreated samples.

Author Contributions

Z.Z.: conceptualization, methodology, software; G.W.: data curation, writing—original draft preparation; J.L.: software, validation; H.W. and L.D.: writing—reviewing and editing. All authors have read and agreed to the published version of the manuscript.

Funding

This work was funded by the financial support from the National Natural Science Foundation of China (22476084).

Institutional Review Board Statement

Not applicable.

Informed Consent Statement

Informed consent was obtained from all subjects involved in the study.

Data Availability Statement

Data sharing is not applicable to this article as no new data were created or analyzed in this study.

Conflicts of Interest

The authors declare no conflict of interest.

Use of AI and AI-Assisted Technologies

No AI tools were utilized for this paper.

References

1. Zheng, Y.F.; Su, Y. Interface-Enhanced Oxygen Vacancies of $CoCuO_x$ Catalysts *in Situ* Grown on Monolithic Cu Foam for VOC Catalytic Oxidation. *Environ. Sci. Technol.* **2022**, *56*, 1905–1916.
2. Yang, Y.; Si, W.Z. Oxygen Vacancy Engineering on Copper-Manganese Spinel Surface for Enhancing Toluene Catalytic Combustion: A Comparative Study of Acid Treatment and Alkali Treatment. *Appl. Catal. B Environ.* **2024**, *340*, 123142.
3. Zhang, K.; Ding, H.L. Research Progress of a Composite Metal Oxide Catalyst for VOC Degradation. *Environ. Sci. Technol.* **2022**, *56*, 9220–9236.
4. Feng, Y.; Wang, C.C. Catalytic Stability Enhancement for Pollutant Removal via Balancing Lattice Oxygen Mobility and VOCs Adsorption. *J. Hazard. Mater.* **2022**, *424*, 127337.

5. Zhang, B.; Shen, Y. Boosting Ozone Catalytic Oxidation of Toluene at Room Temperature by Using Hydroxyl-Mediated MnO_x/Al_2O_3 Catalysts. *Environ. Sci. Technol.* **2023**, *57*, 7041–7050.
6. Li, L.M.; Wahab, M.A. Pt-Modulated $CuMnO_x$ Nanosheets as Catalysts for Toluene Oxidation. *ACS Appl. Nano Mater.* **2021**, *4*, 6637–6647.
7. Ning, H.Q.; Xie, K.Y. Boosting Sulfur Tolerance in Pd/Beta Zeolite Catalyst for Toluene Oxidation: The Role of CeO_2. *J. Rare Earths* **2025**, *43*, 1635–1642.
8. Nunotani, N.; Saeki, S. Novel Catalysts Based on Lanthanum Oxyfluoride for Toluene Combustion. *Mater. Lett.* **2020**, *258*, 126802.
9. Qi, Y.; Yang, Z.Y. Platinum-Copper Bimetallic Nanoparticles Supported on TiO_2 as Catalysts for Photo-Thermal Catalytic Toluene Combustion. *ACS Appl. Nano Mater.* **2022**, *5*, 1845–1854.
10. Wu, C.; Liu, Q.L. Insights into the Surface Structure-Sensitive Photocatalytic Oxidation of Gaseous Toluene on Pd/TiO_2 Catalysts. *Chem. Eng. J.* **2023**, *475*, 146294.
11. Shen, Y.; Liu, S.S. Photocatalytic Degradation of Toluene by a TiO_2 p-n Homojunction Nanostructure. *ACS Appl. Nano Mater.* **2022**, *5*, 18612–18621.
12. Shan, C.P.; Hou, X.Y. Recent Advances of Gaseous Pollutant Catalytic Oxidation over Precious Metal Catalysts with SO_2 Exposure. *Environ. Sci. Technol.* **2025**, *59*, 2348–2367.
13. Xie, K.Y.; Wang, Z. Synthesis of Quantitative Sulfur-Poisoned $Pd/\gamma\text{-}Al_2O_3$ and Its Deactivation Mechanism for Catalytic Combustion of Toluene. *Appl. Catal. A Gen.* **2022**, *639*, 118641.
14. Wang, Y.F.; Liu, X.Y. Promotion of Catalytic Performance of Pd/Al_2O_3 for o-Xylene Oxidation by Morphological Control. *Chem. Eng. J.* **2023**, *472*, 145013.
15. Xu, F.P.; Wang, J. Catalytic Performance and Mechanism of Toluene Oxidation in High Humidity over the Mesoporous Titania-Ceria-Supported Pt or Pd Catalysts. *Appl. Catal. A Gen.* **2025**, *699*, 120277.
16. Wang, S.; Wang, S. CO Oxidation with Pt Catalysts Supported on Different Supports: A Comparison of Their Sulfur Tolerance Properties. *Appl. Catal. A Gen.* **2023**, *654*, 119083.
17. Hao, X.H.; Wu, S.N. *In Situ* Reaction-Induced Strong Metal-Support Interaction to Enhance Catalytic Performance and Stability of Toluene Oxidation. *Sep. Purif. Technol.* **2025**, *358*, 130266.
18. Gil, S.; Garcia-Vargas, J.M. Catalytic Oxidation of Propene over Pd Catalysts Supported on CeO_2, TiO_2, Al_2O_3 and M/Al_2O_3 Oxides (M = Ce, Ti, Fe, Mn). *Catalysts* **2015**, *5*, 671–689.
19. Li, G.; Shen, K. SO_2 Poisoning Mechanism of the Multi-Active Center Catalyst for Chlorobenzene and NO_x Synergistic Degradation at Dry and Humid Environments. *Environ. Sci. Technol.* **2021**, *55*, 13186–13197.
20. Luo, N.; Gao, F. Hierarchical Structured Ti-Doped CeO_2 Stabilized $CoMn_2O_4$ for Enhancing the Low-Temperature NH_3-SCR Performance within Highly H_2O and SO_2 Resistance. *Appl. Catal. B Environ.* **2024**, *343*, 123442.
21. Jiang, B.S.; Xie, K.Y. Study on the Mechanism of Sulfur Poisoning in Toluene Catalyzed by $Co_3O_4/\gamma\text{-}Al_2O_3$ Sulfur Tolerant Catalyst Containing Spinel Structure. *J. Environ. Chem. Eng.* **2023**, *11*, 10518.
22. Payan, A.; Soltan, J. Intensified Catalytic Decomposition of Acetone at Room Temperature Using a Ag-Modified CeO_2–Al_2O_3 Binary Metal Oxide Support: Enhancing Synergies, Role of Relative Humidity, and *in Situ* Mechanistic Interpretation. *Ind. Eng. Chem. Res.* **2025**, *64*, 8047–8063.
23. Payan, A.; Soltan, J. Impact of Support on Acetone Oxidation by Ag@S (S = CeO_2, Al_2O_3, ZSM-5) Catalysts under VUV Illumination at Room Temperature: Improving Synergy, Influence of Relative Humidity, and *In-Situ* Mechanistic Studies. *J. Environ. Chem. Eng.* **2025**, *13*, 117334.
24. Escandón, L.S.; Ordóñez, S. Sulphur Poisoning of Palladium Catalysts Used for Methane Combustion: Effect of the Support. *J. Hazard. Mater.* **2008**, *153*, 742–750.
25. Ding, Y.; Wang, S. Investigation of Supported Palladium Catalysts for Combustion of Methane: The Activation Effect Caused by SO_2. *Chem. Eng. J.* **2020**, *382*, 122969.
26. Murindababisha, D.; Yusuf, A. Low-Temperature Catalytic Oxidation of Toluene Using CeO_2@MIL-101(Fe): Stability against Water and SO_2. *Process Saf. Environ. Prot.* **2025**, *197*, 107005.
27. Wang, Z.; Xie, K.Y.; Zheng, J.; et al. Studies of Sulfur Poisoning Process via Ammonium Sulfate on $MnO_2/\gamma\text{-}Al_2O_3$ Catalyst for Catalytic Combustion of Toluene. *Appl. Catal. B Environ.* **2021**, *298*, 120595.
28. Feng, Z.T.; Ren, Q.M. Effect of CeO_2 Morphologies on Toluene Catalytic Combustion. *Catal. Today* **2019**, *332*, 177–182.
29. Wang, Z.W.; Li, S.X. Supported Ultralow Loading Pt Catalysts with High H_2O-, CO_2-, and SO_2-Resistance for Acetone Removal. *Appl. Catal. A Gen.* **2019**, *579*, 106–115.
30. Xiang, N.; Han, X.J. Size Effect of $\gamma\text{-}Al_2O_3$ Supports on the Catalytic Performance of $Pd/\gamma\text{-}Al_2O_3$ Catalysts for HCHO Oxidation. *Mol. Catal.* **2020**, *494*, 111112.
31. Xu, J.Y.; Zhu, L.H. SiO_2-Supported Pd Nanoparticles for Highly Efficient, Selective and Stable Phenol Hydrogenation to Cyclohexanone. *Mol. Catal.* **2023**, *538*, 112975.

32. Bazin, P.; Saur, O. A Thermogravimetric and FT-IR Study of the Reduction by H_2 of Sulfated $Pt/Ce_xZr_{1-x}O_2$ Solids. *Appl. Catal. B Environ.* **2009**, *90*, 368–379.
33. Zhang, X.F.; Liu, Y. Catalytic Performance and SO_2 Resistance of Zirconia-Supported Platinum-Palladium Bimetallic Nanoparticles for Methane Combustion. *Catal. Today* **2022**, *402*, 138–148.
34. Huang, Z.; Fan, Z. Enhanced NO_x Catalytic Reduction by NH_3 over Polymeric Sulfur Species in CeO_2 via Tailoring Ce–O Bonds. *Inorg. Chem.* **2025**, *64*, 20517–20526.
35. Srinithi, S.; Chen, S.M. Fabrication of N-Rich Graphitic Carbon Nitride Supported CeO_2 for Improved Photocatalytic Charge Separation and Electrochemical Electron Transfer Properties. *Surf. Interfaces* **2023**, *39*, 102877.
36. Arooj, A.; Tahir, K. One-Step Fabrication of Surfactant Mediated Pd/SiO_2, a Prospect toward Therapeutic and Photocatalytic Applications. *Inorg. Chem. Commun.* **2022**, *142*, 109692.
37. Gao, Q.; Dong, C.Q. Effect of the Fe_2O_3@TiO_2 Core-Shell Structure on CO Catalytic Oxidation and SO_2 Poisoning Resistance. *Mol. Catal.* **2023**, *547*, 113308.
38. Heshmatpour, F.; Aghakhanpour, R.B. Synthesis and Characterization of Superfine Pure Tetragonal Nanocrystalline Sulfated Zirconia Powder by a Non-Alkoxide Sol-Gel Route. *Adv. Powder Technol.* **2012**, *23*, 80–87.
39. Dun, Y.H.; Liu, Y.F. Pt^0-$MnSO_4$ Active Centers on Modified $SmMn_2O_5$ Mullite Oxides for Efficient Propane Oxidation. *Appl. Catal. B Environ.* **2025**, *371*, 125223.
40. Li, J.; Wu, Y. Carbothermal Reduction Synthesis of Superfined TiC Powders from $TiOSO_4$. *Adv. Mater. Res.* **2011**, *415*, 510–513.
41. Kinnunen, N.M.; Hirvi, J.T. Case Study of a Modern Lean-Burn Methane Combustion Catalyst for Automotive Applications: What Are the Deactivation and Regeneration Mechanisms? *Appl. Catal. B Environ.* **2017**, *207*, 114–119.
42. Jiang, D.; Khivantsev, K. Low-Temperature Methane Oxidation for Efficient Emission Control in Natural Gas Vehicles: Pd and Beyond. *ACS Catal.* **2020**, *10*, 14304–14314.
43. Wang, L.; Sun, Y.G. Electron Donation Promotes the Dual Activation of Lattice Oxygen and Molecular Oxygen: The Pt-Pd/CeO_2 Catalyst Efficiently Catalyzes Toluene. *J. Catal.* **2023**, *428*, 115133.
44. Liu, T.; Yan, H.M. Promoting Pd/Al_2O_3 Catalysts for Toluene Combustion by DBD Plasma Treating in Different Working Gas Atmospheres. *Catal. Today* **2023**, *421*, 114177.
45. Zhang, W.J.; Liu, G.F. Temperature Sensitivity of the Selective Catalytic Reduction (SCR) Performance of Ce-TiO_2 in the Presence of SO_2. *Chemosphere* **2019**, *243*, 125419.
46. Byun, M.Y.; Park, D.W. Effect of Oxide Supports on the Activity of Pd Based Catalysts for Furfural Hydrogenation. *Catalysts* **2020**, *10*, 837.
47. Fan, L.P.; Zhang, J. Ceria Morphology-Dependent Pd-CeO_2 Interaction and Catalysis in CO_2 Hydrogenation into Formate. *J. Catal.* **2021**, *397*, 116–127.
48. Liu, X.G.; Zhang, X. Pd Nanoparticles Supported on N-Doped TiO_2 Nanosheets: Crystal Facets, Defective Sites, and Metal-Support Interactions Boost Reforming of Formaldehyde Solution for Hydrogen Production. *Langmuir* **2022**, *38*, 13532–13542.